The Journal of Immunology, 2025, **00**, 1–17
https://doi.org/10.1093/jimmun/vkaf250
Research Article

Glutamine synthetase deficiency enhances CD8 T cell survival and stress resilience in the tumor microenvironment

Emilie L. Fisher-Gupta[1,2], Emma S. Hathaway[1], Jeffrey M. Perera[1], Erin Q. Jennings[3], Channing Chi[1,2], Allison E. Sewell[1], Spenser H. Stone[1], Jason E. Muka[1], Rachael C. Sinard[1,4], Joseph A. DeCorte[2,5,6], Heidi Chen[7], John T. Wilson[1,4,8], Jens Meiler[5,6,9], and Jeffrey C. Rathmell[1,8,10,*]

[1]Department of Pathology, Microbiology, and Immunology, Vanderbilt University Medical Center, Nashville, TN, United States
[2]Medical Scientist Training Program, Vanderbilt University, Nashville, TN, United States
[3]Department of Medicine, Vanderbilt University Medical Center, Nashville, TN, United States
[4]Department of Chemical and Biomolecular Engineering, Vanderbilt University, Nashville, TN, United States
[5]Center for Structural Biology, Vanderbilt University, Nashville, TN, United States
[6]Department of Chemical and Physical Biology, Vanderbilt University, Nashville, TN, United States
[7]Department of Biostatistics, Vanderbilt University Medical Center, Nashville, TN, United States
[8]Vanderbilt Center for Immunobiology, Vanderbilt University Medical Center, Nashville, TN, United States
[9]Institute for Drug Discovery, Institute for Computer Science, Wilhelm Ostwald Institute for Physical and Theoretical Chemistry, University Leipzig, Leipzig, Germany
[10]Ben May Department for Cancer Research, Ludwig Center at the University of Chicago, Chicago, IL, United States

*Corresponding author: Ben May Department for Cancer Research, Ludwig Center at the University of Chicago, Chicago, IL 60637, United States.
Email: rathmell@uchicago.edu

Abstract

Cellular immunotherapy has revolutionized the treatment of hematologic malignancies yet has had limited success in the solid tumor microenvironment (TME). While insufficient nutrients can lead to T cell metabolic stress in the TME, the glutamine antagonist DON can paradoxically enhance antitumor immunity. Because DON inhibits both essential and nonessential enzymes whose impairment may contribute to dose-limiting toxicities, mechanisms underlying DON-induced antitumor activity have remained unclear. Here, we aimed to identify specific DON targets that increase T cell antitumor activity and test if more selective inhibition of glutamine metabolism could replicate the effects of DON with reduced toxicity. CRISPR screening in the TME of DON-relevant glutamine metabolizing enzymes identified some targets that were essential in tumor-infiltrating CD8 T cells, but that tumor-infiltrating CD8 T cells lacking the DON target glutamine synthetase (GS) were enriched. Upon adoptive T cell transfers, GS-deficient $CD8^+$ T cells displayed improved survival, a higher proportion $TCF\text{-}1^+$ Tox^- stem-like cells, and greater antitumor and memory function. GS converts glutamate to glutamine and GS-deficient cells exhibited increased intracellular glutamate and reduced glutathione levels, which correlated with enhanced mitochondrial respiration and resistance to reactive oxygen species. Pharmacological inhibition of GS reduced tumor burden in multiple orthotopic murine tumor models in a manner dependent on adaptive immunity. Our findings establish GS as a key metabolic regulator of $CD8^+$ T cells stress resilience in the TME. By preserving intracellular glutamate, GS inhibition reprograms T cells for improved survival and function, offering a promising therapeutic strategy to enhance immune-based cancer treatments.

Keywords: T cell, immunometabolism, glutamine, antitumor immunity, glutamine synthetase

Introduction

Cancer treatment has been transformed for many patients by the advent of cellular immunotherapies. These therapies, including chimeric antigen receptor T cell therapy and adoptive T cell therapy with tumor-specific T cells, are now standard care for several hematologic malignancies, with recent FDA approval for treating unresectable metastatic melanoma.[1,2] However, cell-based immune therapies remain largely limited to these applications. While chimeric antigen receptor T cell therapies are highly effective in liquid tumors, their efficacy in solid tumors is poor due in part to the suppressive tumor microenvironment (TME), which poses a substantial barrier to immunotherapy. The TME creates a hostile environment for infiltrating T cells through factors such as nutrient competition, hypoxia, immunosuppressive signaling, changing temperatures with poor blood flow and inflammation, and metabolic reprogramming, leading to T cell exhaustion and dysfunction.[3,4] A critical factor driving the suppressive nature of the TME is the limited availability of metabolites essential for cellular metabolic programs, such as low glucose preventing T cell glycolysis and antitumor signaling through the intermediate phosphoenolpyruvate.[5,6]

Among these altered nutrients, glutamine is an abundant, conditionally essential amino acid that is vital for a wide range of metabolic pathways. These include essential roles in nucleotide synthesis, glycosylation, mitochondrial metabolism, and redox balance. Given the potential to harm cancer cells of blocking these pathways, targeting glutamine metabolism has been a focus of research since the 1950s, when the pan-glutamine inhibitor DON was first tested as an antitumor agent.[7] Although an effective antitumor agent, DON led to significant toxicities due to inhibition of a wide range of glutamine

Received: March 2, 2025. **Revised:** August 16, 2025. **Accepted:** August 25, 2025

metabolizing enzymes. Indeed, dose limiting gastrointestinal toxicities led to the suspension of early clinical trials. A promising approach to overcome this barrier has been to develop DON prodrugs that selectively activate within the TME.[8–12] However, the broad-based inhibition of glutamine metabolism by DON nevertheless exerts pleiotropic effects that affect not only tumor cells, but also tumor infiltrating dendritic cells, myeloid cells, and T cells. Interestingly, it is now clear that the antitumor effect of DON is part due to enhanced immune function.[13] The negative effects of DON on cancer cells but positive effects to promote antitumor immunity likely reflect the polypharmacology of DON to inhibit both essential and potentially inhibitory metabolic processes and the balance of those processes on different cell types. Indeed, the overall increased T cell function suggests DON provides an overall fitness advantage to T cells despite inhibition of some critical enzymes that may restrain antitumor immunity.

We sought to identify specific glutamine metabolizing enzymes that may selectively enhance $CD8^+$ T cell function in the TME. To explore how to target glutamine metabolism in antitumor immunity more specifically than DON, we performed an in vivo CRISPR screen on $CD8^+$ T cells within the TME using a glutamine transport and metabolism guide RNA library. While essential enzymes for glutamine metabolism were identified to reduce T cell fitness when deleted, glutamine synthetase (GS) deficiency uniquely improved $CD8^+$ T cell fitness in the TME. We further demonstrate that pharmacological inhibition or genetic deletion of GS increased intracellular glutamate stores in $CD8^+$ T cells, enhancing mitochondrial metabolism, resistance to reactive oxygen species (ROS), and overall tumor control. Importantly, GS-deficient cells had increased effector function while retaining expression of markers of memory and stemness. This work highlights that selective targeting of GS may yield the antitumor benefits of DON without the dose-limiting toxicities and provide a potential target for future therapeutic development.

Methods

Mice

Thy1.1 (000406), Cas9 transgenic (026179), OT-I transgenic (003831), CD4-Cre (017336), and *Rag1*$^{-/-}$ (002216) mice were obtained from the Jackson Laboratory and maintained in Vanderbilt University Medical Center animal facilities. Cas9 and OT-I transgenic mice were crossed until double homozygosity and used in all CRISPR experiments. *Glul* fl/fl mice were a generous gift from Saverio Tardito at the University of Glasgow and bred with CD4-Cre mice to obtain T cell specific GS knockout (KO) mice.[14] Wild-type (WT) CD4-Cre negative *Glul* fl/fl mice were compared with knockout CD4-Cre positive *Glul* fl/fl littermates. All mice were on the C57Bl/6J background, and both male and female mice were utilized in experiments. All mouse procedures were performed under Vanderbilt University Medical Center Institutional Animal Care and Use Committee–approved protocols and conformed to all relevant regulatory standards. Mice were housed in ventilated cages with at most 5 animals per cage and provided ad libitum water and food. For injectable tumor models, 6- to 12-wk old mice were used.

Media

T cells were maintained in RPMI 1,640 supplemented to a final concentration of 0.6 mM glutamine, 10% fetal bovine serum (FBS), 10 mM HEPES, 50 μM BME, and penicillin-streptomycin (100 U/mL). Plat-E retroviral packaging cell line was maintained in DMEM media supplemented with 10% FBS, 100 U/mL penicillin/streptomycin, 1 μg/mL puromycin, and 10 μg/mL blasticidin to maintain expression of viral packaging genes. All tumor lines were maintained in DMEM supplemented with 10% FBS.

Cancer cell lines

MC38-Ova cells were generated as described previously,[15] PyMT cells were a generous gift from Ann Richmond at Vanderbilt University Medical Center, and HKP1-Ova cells were gifted from Vivek Mittal at Cornell University and described previously.[16] In each tumor model, cells were plated at 1×10^6 cells in a 10 cm TC-treated dish 2 d prior to injection. MC38-Ova cells were trypsinized, washed twice in phosphate-buffered saline (PBS), and 1×10^6 cells were injected subcutaneously in 100 to 200 μL of PBS on mouse flanks. For tumor rechallenge experiments, 5×10^6 cells were injected subcutaneously into the opposite flank as the first injection. For orthotopic PyMT models, 1×10^6 cells were injected into the mammary fat pad. A total of 100,000 cells were injected intravenously for the HPK1-Ova lung tumor model.

MC38-Ova and PyMT injected mice were euthanized (survival endpoint) for 2 cm tumor dimension, ulceration, or weight loss >10%. Tumor calipering and mouse weighing was performed 3 times a week and blinded to treatment group. HPK1-Ova tumor growth was monitored using the PerkinElmer IVIS Spectrum. Mice were injected with 150 mg/kg D-luciferin (Promega; P1043) for 10 min prior to imaging. Quantification was performed using PerkinElmer's Living Image software, Version 4.7.2.

T cell culture

Glul fl/fl CD4-Cre(+) and Cre(−) splenocytes were isolated, passed through a 70 μm filter, and activated in cRPMI supplemented with 100 U/mL recombinant human interleukin (IL)-2 (National Cancer Institute; Ro 23-6019) on plates coated with 3 μg/mL αCD3/28 (clone145-2C11 [Invitrogen; 16-0031-86], clone 37.51 [Invitrogen; 16-0281-86]). Cells were collected, washed with PBS, and replated on TC-treated plates after 48 h of activation. For L-methionine sulfoximine (MSO) experiments, cRPMI was additionally supplemented with indicated concentration of MSO or equal volume of PBS.

Tumor digestions

MC38-Ova and PyMT tumors were chopped, mechanically dissociated on the Miltenyi gentleMACS Octo Dissociator and digested in 870 U/mL DNase I (Sigma-Aldrich; D5025) and 218 U/mL collagenase IA (Sigma-Aldrich; C2674) at 37 °C for 30 min. For HKP1-Ova tumors, collagenase IV (Worthington; LS004188) was used in place of type 1A. Tumor cells were then passed through a 70 μm filter and tumor-infiltrating $CD8^+$ T lymphocytes (TILs) were subsequently extracted using Miltenyi CD45 or CD8 isolation kits (130-110-618 and 130-116-478) per the manufacturer's instructions.

Flow cytometry

Single-cell suspensions were incubated in F_c block (1:50; BD; 553142) for 15 min at room temperature (RT), stained for

surface markers for 30 min at RT, washed with FACS buffer (PBS $^{+}$2% FBS) once, and resuspended in FACS buffer for analysis on a Miltenyi MACSQuant Analyzer 16. For intracellular staining, the eBioscience Foxp3/transcription factor staining buffer kit (Fisher 00-5523-00) was used. For intracellular cytokine staining, single cell suspensions were incubated for 4 hr at 37 °C 5% CO_2 in supplemented RPMI with PMA (50 ng/mL, Sigma Aldrich P8139), ionomycin (750 ng/mL, Sigma Aldrich I0634), and GolgiPlug (1:1000, BD 555029), and processed using the BD Cytofix/Cytoperm Fixation and Permeabilization Solution (Thermo Fisher Scientific; BDB554722). Surface staining was performed as described previously. Cells were fix/permed for 30 min at 4 °C and then stained for intracellular markers overnight at 4 °C. Staining occurred in 50 μL total volume. In noted experiments, viable transduced cells were sorted using a FACSAria III Cell Sorter in the Vanderbilt Flow Cytometry Shared Resource. The Vanderbilt Flow Cytometry Shared Resource is supported by the Vanderbilt Ingram Cancer Center (P30 CA068485) and the Vanderbilt Digestive Disease Research Center (DK058404). Antibodies used were CD4 APC (1:400; RM4-5; eBioscience; 17-0042-82), CD4 eF450 (1:400; GK1.5; eBioscience; 48-0041-82), CD4 SB600 (1:400; GK1.5; eBioscience; 63-0041-82), CD8a eF450 (1:400; 53.6-7; eBioscience; 48-0081-82), CD8a SB600 (1:600; 53-6.7; eBioscience; 63-0081-82), CD45 FITC (1:300; S18009F; BioLegend; 157214), CD45.1 FITC (1:300, A20; BioLegend; 110706), CD45.2 FITC (1:300, 104; BioLegend; 109806), CD62L APC (1:300, MEL-14; eBioscience; 17-0621-82), CD69 APC (1:300; H1.2F3; BioLegend; 104514), CD69 PE-Cy7 (1:300; H1.2F3; BioLegend; 104512), Granzyme-B PE (1:200; NGZB; eBioscience; 12-8898-82), IFN-γ APC (1:200; XMG1.2; BioLegend; 505809), PD-1 (CD279) PE-Cy7 (1:300; 29F.1A12; BioLegend; 135216), TCF1/TCF7 AF647 (1:100; C63D9; Cell Signaling Technology; 6709S), TCF1/TCF7 PacBlue (1:100; C63D9; Cell Signaling Technology; 9066S), TCF1/TCF7 PE-Cy7 (1:100; C63D9; Cell Signaling Technology; 90511S), THY1.1 SB600 (1:600; HIS51; eBioscience; 63-0900-82), TNF VF450 (1:200; MP6-XT22; BD Biosciences; 560655), TNF-a PE-Cy7 (1:200; MP6-XT22; BioLegend; 506324), and TOX APC (1:100; REA473, Miltenyi Biotec; 130-118-335). The NIH Tetramer Core Facility provided the SIINFEKL PE tetramer (1:1000). CellTrace Violet (CTV) (Thermo Fisher Scientific; C34557) was used at 1:1,000 for cell proliferation assays. Mitochondrial mass was measured with 200 nM MitoTracker Green FM (Invitrogen; M7514) and mitochondrial membrane potential was measured with 150 nM TMRE (Lifetech; T-669) staining for 30 min at 37 °C 5% CO_2 in PBS. Flow cytometry data were analyzed using FlowJo v10.7.1 (BD).

Virus production

Glutamate CRISPR library DNA was synthesized as reported previously.[17] Single guide RNAs (sgRNAs) targeting *Glul* and nontargeting controls (NTCs) were cloned into pMx-U6-sgRNA-BFP or pMx-U6-sgRNA-Thy1.1 retroviral vectors, grown in One Shot TOP10 chemically competent cells (Thermo Fisher Scientific; C404010), and extracted using Qiagen miniprep kit (27104). The *Glul* sequence was TATTTCTAGAGACCAACTTG. The NTC sequence was GCTTTCACGGAGGTTCGACG.

DNA was transfected into Plat-E retroviral packaging cell line using Polyplus jetPRIME DNA and small interfering RNA transfection reagent (VWR; 89129-922). Media was changed 24 h post-transfection, and viral supernatant was collected after an additional 48 h of culture.

In vivo CRISPR screen

Splenocytes isolated from Cas9; OT-I double transgenic mice were activated for 48 h in cRPMI with SIINFEKL peptide (10 ng/mL; Sigma-Aldrich; S7951) and recombinant human IL-2 (100 IU/mL). At 48 h, CD8^{+} cells were isolated via negative magnetic separation (Miltenyi; 130-104-075) per the manufacturer's instructions.

For transduction, viral supernatants generated as described previously were centrifuged at 2,000 *g* for 2 h at 32 °C on retronectin-coated plates (Takara Bio; T100A). Activated T cells were then layered onto plates and centrifuged for an additional 15 min. Cells were collected and transduction efficiency was measured by flow cytometry after 24 h. In parallel, *Rag1*$^{-/-}$ mice were injected subcutaneously on the right flank with 1×10^6 MC38-Ova cells. On tumor day 10 mice were injected with 10×10^6 OT-I; Cas9 cells with a transduction efficiency of approximately 20%.

Following 7 d of in vivo selection, mice were sacrificed, and tumors and spleens were collected. Tumors were dissociated as described previously. Flow cytometry was performed on the recovered cell fraction to measure transduction efficiency, and at least a 1,000-fold representation of the library was confirmed to ensure robust coverage of the library. Recovered cells were sequenced by VANTAGE (Vanderbilt Technologies for Advanced Genomics) and analyzed using the MAGeCK (Model-based Analysis of Genome-wide CRISPR-Cas9 Knockout) method for statistical analysis.[18]

Adoptive transfer

For 1:1 *Glul*:NTC tumor experiments, splenocytes from OT-I; Cas9 transgenic mice were activated as described previously. Following 48 h of activation, cells were transduced, as previously, with *Glul*-sgRNA or NTC-sgRNA in plasmids with either BFP or Thy1.1 expression. After 24 h, transduction efficiency was measured by flow cytometry, and cells were combined such that the number of cells transduced with *Glul*-sgRNA approximated the number of NTC-sgRNA cells. Injected mix was measured again by flow immediately prior to injection to obtain actual starting ratio. Mice were preconditioned with 5 Gy of radiation the day prior to adoptive cell transfer. Cells were resuspended in PBS and each mouse received 4 to 5×10^6 cells retro-orbitally in a total volume of 100 μL.

For mice treated with either *Glul*-sgRNA or NTC-sgRNA cells, activation and transduction was performed as previously. A total of 48 h after transduction, cells were stained for their respective transduction marker and sorted using a FACSAria III Cell Sorter in the Vanderbilt Flow Cytometry Shared Resource. Cells were then plated in fresh cRPMI with 100 U/mL recombinant human IL-2 for 24 h prior to harvest, resuspended in PBS, and 3×10^6 cells were injected retro-orbitally into tumor-bearing mice.

Pharmacologic treatment

For mice with MC38-Ova tumors treated with DON, injections began on day 18 postinjection when tumors had all become palpable. Mice were treated with daily intraperitoneal injections of 0.5 mg/kg DON or PBS for 5 d. Mice treated

with MSO received 20 mg/kg MSO or PBS intraperitoneal daily for 5 d, beginning 16 d postinjection of PyMT cells or 10 d postinjection of HKP1-Ova cells.

Listeria infection

The 6- to 8-wk-old C57Bl/6J mice were injected retro-orbitally with 1×10^6 OT-I; Cas9 T cells in a 1:1 ratio of cell transduced with *Glul*-sgRNA or NTC-sgRNA, as described in the adoptive transfer section previously. The following day, 1×10^7 CFUs of attenuated *Listeria monocytogenes*–expressing SIINFEKL peptide (*Lm*-Ova) were injected intraperitoneally. Mice were bled via cheek bleed on day 5 following *Lm*-Ova infection for early timepoint flow analysis. On day 30 following initial infection, mice were injected intraperitoneally with a second dose of 1×10^7 CFUs *Lm*-Ova. Mice were euthanized on day 35 for blood, spleen, and lymph node collection and subsequent flow analysis.

Metabolomics

WT or *Glul* fl/fl CD4-Cre $CD8^+$ T cells were isolated and activated as described previously in T Cell Culture. Following activation for 48 h, cells were washed and replated in fresh cRPMI with 100 U/mL IL-2 at a concentration of 1×10^6 cells/mL for an additional 48 h. For MSO treatment, WT cells were treated during this second period with or without 5 mg/mL MSO.

Following this incubation, cells were pelleted in 15 mL conical tubes and washed with PBS. After washing, the pellets were flash-frozen in liquid nitrogen and stored at −80°C until metabolite extraction. To extract metabolites, 1 mL of −80°C 80:20 MeOH: H_2O was added to each pellet, followed by vigorous vortexing. Each sample was spiked with 100 nmol of internal standard (^{13}C-1-Lactate; MilliporeSigma) and incubated at −80°C for 15 min.

Following extraction, precipitated proteins were pelleted at 2,800 *g* for 10 min at 4 °C. The supernatant containing metabolites was transferred to a new 15 mL conical tube and dried under nitrogen gas. Protein pellets were resolubilized and protein concentration was measured via BCA assay (Thermo Fisher Scientific). Dried metabolite extracts were resuspended in 50 µL of a 3:2 mixture of mobile phase A and B (detailed subsequently) and transferred to 1.7 mL Eppendorf tubes. Samples were centrifuged at 16,000 *g* for 10 min at 4 °C to remove insoluble debris.

For liquid chromatography tandem mass spectrometry analysis, 18 µL of each sample was injected into a Shimadzu LC system equipped with a 100 × 2.1 mm, 3.5 µm particle diameter XBridge Amide column (Waters). The mobile phases consisted of mobile phase A, 20 mM NH_4OAc, 20 mM NH_4OH, 5% acetonitrile in water, pH adjusted to 9.45 with NH_4OH; and mobile phase B, 100% acetonitrile. The following gradient was applied at a flow rate of 0.45 mL/min: 2.0 min, 95% B; 3.0 min, 85% B; 5.0 min, 85% B; 6.0 min, 80% B; 8.0 min, 80% B; 9.0 min, 75% B; 10 min, 75% B; 11 min, 70% B; 12 min, 70% B; 13 min, 50% B; 15 min, 50% B; 16 min 0% B; 17.5 min, 0% B; 18 min, 95% B. The column was equilibrated at 95% B for 3 min between each sample. Scheduled MRM was conducted in negative mode with a 120-s detection window using an AB SCIEX 6,500 QTRAP using the following analyte parameters: *m/z* 179 → 89 (RT: 6.9 min) for glucose; *m/z* 333 → 97 (RT: 13.8 min) for fructose 1,6-bisphosphate; *m/z* 185 → 97 (RT: 13.4 min) for 3-phosphoglycerate; *m/z* 167 → 79 (RT: 13.3 min) for phosphoenolpyruvate; *m/z* 87 → 43 (RT: 3.0 min for pyruvate; *m/z* 89 → 43 (RT: 6.0 min) for lactate; *m/z* 90 → 43 (RT: 6.0 min) for ^{13}C-1-lactate [internal standard]; *m/z* 191 → 111 (RT: 13.4 min) for citrate/isocitrate; *m/z* 145 → 101 (RT: 10.3 min) for α-ketoglutarate; *m/z* 117 → 73 (RT: 10.9) for succinate; *m/z* 133 → 115 (RT: 11.4 min) for malate, *m/z* 145 → 127 (RT: 9.5 min) for glutamine; *m/z* 146 → 102 (RT: 11.0 min) for glutamate; *m/z* 132 → 88 (RT: 11.2 min) for aspartate; *m/z* 328 → 134 (RT: 11.1 min) for cyclic AMP; *m/z* 346 → 79 (RT: 12.0 min) for AMP; *m/z* 426 → 328 (RT: 13.3 min) for ADP; *m/z* 506 → 408 (RT: 13.6 min) for ATP; *m/z* 663 → 540 (RT: 12.3 min) for NAD^+; *m/z* 663 → 540 (RT: 13.7 min) for GTP; and *m/z* 422 → 79 (RT: 12.8 min) for GDP. All analytes were quantified via liquid chromatography tandem mass spectrometry using the ^{13}C-1-Lactate internal standard, and results were normalized to the protein content of each sample's cell pellet. Outliers were removed using interquartile range.

Extracellular flux assay

T cells were plated at 150,000 live cells/well with 5 to 7 technical replicates per sample on a Cell-Tak–coated plate (Corning; 354240) in Agilent Seahorse RPMI 1640 supplemented with a final concentration of 10 mM glucose, 1 mM sodium pyruvate, and 0.6 mM glutamine. Cells were analyzed on a Seahorse XFe96 bioanalyzer using either the Mito Stress assay (Agilent; 103015-100) with 1 µM oligomycin, 2 µM FCCP, and 0.5 µM rotenone/antimycin A, or the Substrate Oxidation Stress assay with 30 mM MSO injection prior to oligomycin, FCCP, and rotenone/antimycin A injections. Data were analyzed with Agilent Wave software report generator version 4.03.

CellROX staining

A total of 100,000 cells per well were plated on tissue culture treated flat bottom 96-well plates in 5 µM CellROX Deep Red (Life Technologies; C10422) for 30 min at 37 °C. Cells were transferred to a round bottom 96-well plate and stained for viability prior to flow analysis.

Glutathione measurements

A total of 1×10^6 cells were collected following 48 h of activation as described previously in T Cell Culture. Total and oxidized glutathione (GSSG) were measured using Dojindo quantification kit (G257-10) per the manufacturer's instructions. Reduced glutathione (GSH) was determined by subtracting 2× GSSG from total GSH. Assay was performed in technical triplicate and averaged for each biological replicate.

Hydrogen peroxide killing assays

A total of 100,000 cells per well were plated on tissue culture treated flat bottom 96-well plates in 100 µL cRPMI. H_2O_2 diluted in cRPMI was added to achieve a final concentration of 0, 10, 50, 100, 250, 500, 1,000, and 2,000 µM. Cells were incubated for 3 h at 37 degrees before being transferred to round bottom 96-well plates and stained for flow. Viability for each biological replicate was normalized to the viability of the media-only control wells. For GSH rescue assays, H_2O_2 final concentration was 1,000 µM, and 1 mM GSH was added for the duration of the 3-h incubation.

Immunoblotting

Cells from *Glul* fl/fl CD4-Cre$^+$ (GS KO) or Cre$^-$ (WT) littermate control mice were isolated and activated for 48 h as described previously in T Cell Culture. Cells were lysed with base lysis buffer containing 1% IGEPAL CA-630 (Sigma-Aldrich I8896), 200 mM NaCl, and 50 mM tris (pH 8.0) on ice for 30 min. Lysis buffer was supplemented with the protease inhibitors aprotinin (5 μg/mL; Sigma-Aldrich; A1153), leupeptin (5 μg/mL; Sigma-Aldrich; L2884), sodium fluoride (0.9 mM; Sigma-Aldrich; S7920), dithiothreitol (1 mM; Sigma-Aldrich; 646563), sodium orthovanadate (1 mM; Sigma-Aldrich; S6508), and beta-glycerophosphate (20 mM; Sigma-Aldrich; G9422). Lysates were centrifuged at 13,000 *g* for 15 min at 4 °C to recover supernatant and quantified for protein concentration using protein assay dye reagent concentrate (Bio-Rad; 5000006). Forty micrograms of protein was loaded per well for polyacrylamide gel electrophoresis using Mini-PROTEAN precast polyacrylamide gels (Bio-Rad). Protein immunoblotting was performed using low-fluorescence polyvinylidene difluoride membrane (1620260; Bio-Rad). Transfer was accomplished using the Trans-Blot Turbo Transfer System (Bio-Rad) at 1.3A for 7 min.

Blots were blocked for 1 h using 5% milk in tris-buffered saline + Tween 20 (TBST) before incubation with primary antibody overnight at 4 °C. The blots were washed 3 times with TBST (5 min per wash). Blots were incubated in 5% milk containing anti-rabbit or anti-mouse horseradish peroxidase–linked secondary antibody for 30 min. Blots were washed in TBST, incubated with Pierce ECL Western blotting substrate (Thermo Fisher Scientific; 32106) and then imaged on a GE Healthcare Amersham Imager 600 series. Antibodies used: vinculin (1:10,000; Abcam; ab129002), GS (1:1,000; Invitrogen; MA5-38531). Secondary goat anti-rabbit and goat anti-mouse antibodies were used at a concentration of 1:10,000 (7074S, 7076S; Cell Signaling Technology).

RNA sequencing

CD8$^+$ T cells were isolated from WT or GS KO mice and activated in culture as described previously in T Cell Culture. Cells were replated on days 2 and 4, and cell pellets were collected for RNA extraction on day 5. RNA extraction, library preparation, and sequencing was performed by the VANTAGE core. The messenger RNA (mRNA) library was generated using NEBNext Poly(A) selection kit (New England Biolabs; E7490). Sequencing was performed at multiplex Paired-End 150 bp on the Illumina NovaSeq 6000. Read mapping performed using STAR, gene expression quantification using featureCounts, and differential expression performed using DESeq2. Gene set enrichment analysis was performed using GSEA v4.3.3 Mac App. HALLMARK and IVanalysis of variance gene sets were retrieved from the Broad Institute's MSigDB collections.[19–21]

Data availability

Bulk RNA sequencing data is available through the Gene Expression Omnibus database under accession number GSE290455. Data for all CRISPR screens can be accessed at the Functional ImmunoGenomics resource website.[22]

Results

Glutamine metabolism focused CRISPR screen in the TME identifies GS

We first sought to confirm the antitumor efficacy of pan-glutamine inhibition by DON in our model systems. WT mice were injected with subcutaneous MC38-Ova tumors and treated with daily intraperitoneal injections of DON or vehicle control (PBS). Mice receiving daily injections of DON responded to treatment, with all 10 mice showing significant tumor volume reduction and total tumor elimination was observed in 5 of the mice (Fig. 1A). However, this treatment resulted in significant toxicities, with all 10 mice requiring euthanasia prior to the predefined study endpoint (Fig. 1B). While the specific molecular mechanisms of this dual effect to eliminate tumors yet cause significant toxicity was unknown, the wide range of DON targets and diverse roles for glutamine metabolizing enzymes in tissues such as the gastrointestinal tract likely contributed. The overall effect of DON, therefore, was a balance of positive and negative effects on tumors, other tissues, and antitumor immunity. We sought, therefore, to identify specific DON targets that may more selectively enhance CD8$^+$ T cell function and thus limit toxicity.[7,23]

To probe glutamine metabolizing enzymes that may be critical to CD8$^+$ T cells in the TME, we applied an in vivo forward genetic screen with a CRISPR library containing guide RNAs targeting 32 genes encoding for glutamine transport and glutaminolysis enzymes (Table S1). Activated CD8$^+$ T cells from OT-I; Cas9 double transgenic mice were activated and transduced with this targeted library and injected into MC38-Ova tumor-bearing *Rag1*$^{-/-}$ mice. Following 7 d of in vivo selection pressure, TILs were isolated, DNA was sequenced, and guide abundances were compared with the injected cell fraction (Fig. 1C). Interestingly, cells deficient in *Glul*, the gene encoding GS, were uniquely enriched in all biological replicates, indicating a fitness advantage for these cells (Fig. 1D; Fig. S1A–F). Cells deficient in other DON-targeted enzymes, such as *Gfpt1* and *Ppat*, showed a survival disadvantage in the TME, emphasizing the polypharmacology of DON and importance to identify and specifically target the enzymes that selectively increase TIL antitumor function.

To validate the CRISPR screen findings, Cas9; OT-I transgenic CD8$^+$ T cells were transduced sgRNAs for *Glul* or an NTC, respectively. Cells transduced with the *Glul* guides were labeled with a Thy1.1 marker while NTC cells were labeled with BFP, to allow both populations to be tracked in a single mouse and compare if *Glul*-deficient CTLs had a fitness advantage in the TME compared with control OT-I cells. While subcutaneous MC38-Ova tumors were used for our initial screen due to the requirement for maximal TIL recovery, we sought to confirm the importance of *Glul* an orthotopic tumor setting using HKP1-Ova cells—a lung adenocarcinoma model.[16] Mice were injected intravenously with HKP1-Ova cells to seed lung tumors. HKP1-Ova tumor-bearing mice were then treated with a 1:1 mix of *Glul* KO Thy1.1$^+$ and NTC BFP$^+$ OT-I cells. After 7 d, tumors were harvested and the ratio of *Glul* KO: NTC TIL had increased to greater than to 2:1 (Fig. 1F, G; example gating scheme in Fig. S2), indicating a survival advantage in the *Glul*-deficient cells that recapitulated our CRISPR screen results. Importantly, *Glul* KO cells injected into non–tumor-bearing mice and recovered from healthy lungs (Fig. 1G) or from spleens of tumor-bearing mice (Fig. S1G) showed no advantage. The survival advantage of GS-deficiency was, therefore, specific to the TME.

Given the fitness advantage of GS KO cells in our initial CRISPR screen and mixed cell transfers, GS-deficient CD8$^+$

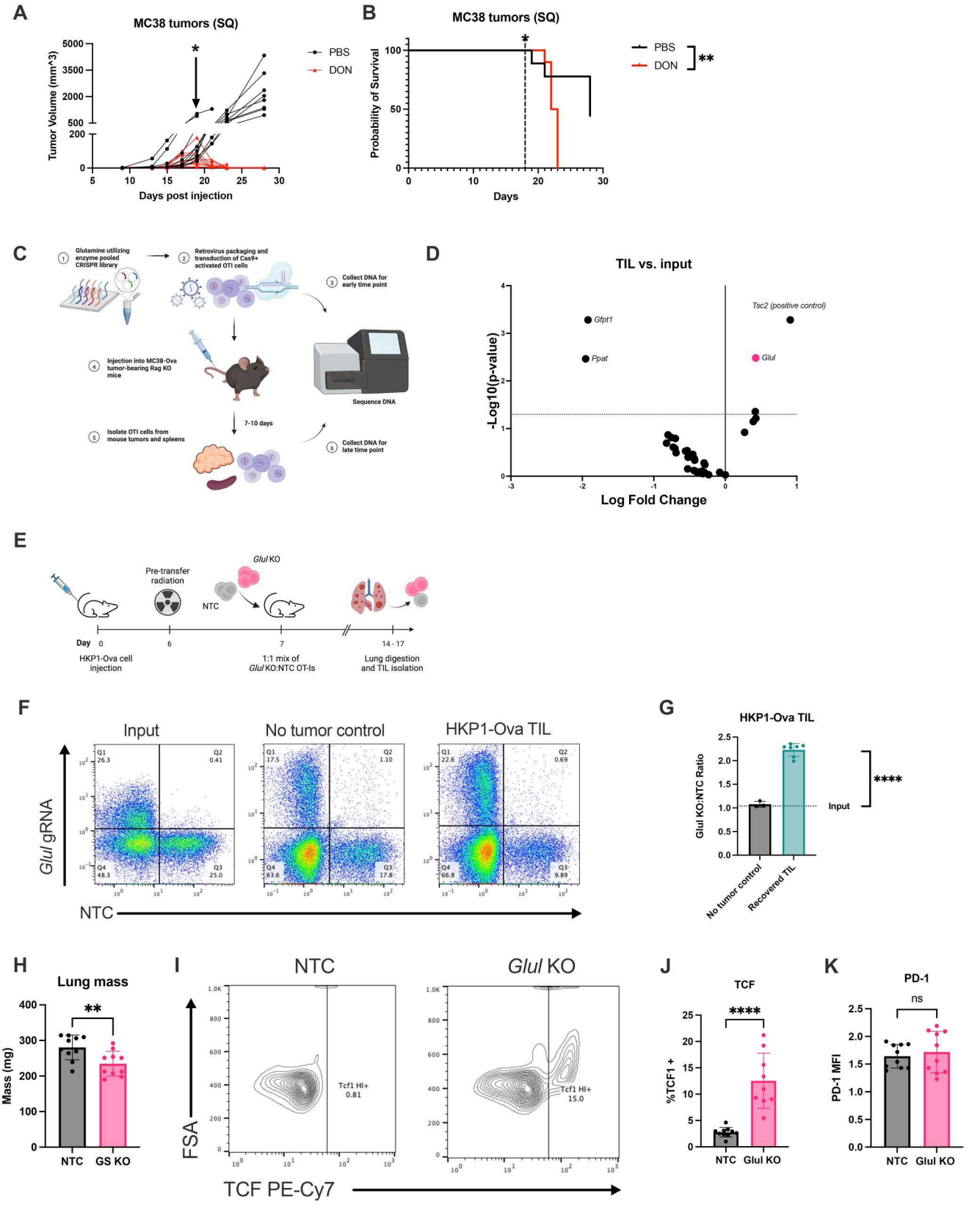

Figure 1. In vivo CRISPR screen identifies target gene *Glul*. (A) Growth curve for subcutaneous MC38-Ova tumors in mice treated intraperitoneally with PBS (black) or DON (red). The asterisk indicates treatment start date (day 18 postinjection). n = 10 per treatment group. (B) Kaplan-Meier survival curve for mice in panel A. (C) Experimental scheme of in vivo CRISPR screen. (D) Representative volcano plot showing enriched and depleted guides in the recovered TIL compared with injected cell population. Statistical analysis performed by MAGeCK, representative for 7 biological replicates over 2 independent experiments. (E) Schematic of 1:1 target validation HKP1-Ova tumor model. (F) Representative flow plots showing relative populations of cells transduced with *Glul* gRNA (*Glul* KO) or NTC gRNA that were injected (input), recovered from lungs without tumors, or recovered from HKP1-Ova tumors (left to right). (G) Quantification of ratio of recovered cells expressing *Glul* vs NTC gRNA from HKP1-Ova tumors (n = 7) or no tumor control lungs (n = 3). A one-sample *t* test used to determine if recovered ratios were significantly different than expected (input) ratio (dashed line). (H) Lung mass as a

(continued)

Figure 1. Continued
proxy for tumor burden. n = 10 per group. (I) Representative flow plots showing TCF-1$^+$ population, gated on live CD8$^+$ T cells, from mice treated with NTC or GS KO mice (left to right). n = 10 per group, quantified in panel J. (K) PD-1 geometric mean florescence intensity (MFI) of recovered CD8$^+$ T cells, as measured by flow. Statistically significant results are labeled. *$P < 0.05$, **$P < 0.01$, *** $P < 0.001$, ****$P \leq 0.0001$. Log-rank (Mantel-Cox) test used in panel B. Mann-Whitney test used in panels H, J, and K.

T cells were directly tested in an adoptive T cell therapy model. Thy1.1$^+$ cells transduced with either *Glul* sgRNA or NTC sgRNA were sorted and transferred into mice bearing HKP1-Ova tumors that had received conditioning radiation the day prior. Lungs isolated from mice treated with GS-deficient CTLs displayed a significantly lower tumor burden, using lung mass a validated unbiased proxy for tumor burden (Fig. 1H).[24] While PD-1 expression did not differ on recovered TIL, the TCF-1$^+$ progenitor-like T cell (Tpex) population was markedly increased in the GS-deficient population (Fig. 1I and J). These results raise the possibility that targeting GS may result in a longer-living, less exhausted, T cell product.

GS deficiency does not significantly alter CD8$^+$ T cells in nondisease context

To further investigate the effects of GS KO in T cells in vivo, we generated a conditional KO mouse strain using *Glul*-floxed mice with a Cre recombinase driven by the CD4 promoter (Fig. 2A). GS deficiency in CD8$^+$ T cells was confirmed in this model via mRNA levels from RNA sequencing data and a western blot showing absence of protein in GS KO mice (Fig. 2B, C). In all experiments, cells derived from GS KO mice are compared with Cre$^-$ littermate control mice (WT). Importantly, no overt phenotypes were observed in GS KO mice. All mice appeared healthy, and no differences in growth were observed.

To characterize the effect of T cell-specific GS KO, thymocyte, splenocyte, and circulating lymphocytes were isolated from healthy, untreated GS KO and WT littermate control adult mice. RPMI medium containing 0.6 mM L-glutamine rather than the superphysiological 2 mM concentration in most RPMI formulations was used for all in vitro experiments to approximate the low glutamine levels found in many TMEs.[13] This physiological concentration more closely approximates levels found in human blood, which range from 0.5 to 0.8 mM.[25] At baseline, no differences were observed in thymocyte number, splenocytes, ratio of CD4: CD8$^+$ T cells, or viability, activation, and proliferation upon stimulation ex vivo (Fig. 2D–H). Importantly, GS KO cells proliferated normally, indicating the relative abundance of GS KO cells in the previous tumor models was not simply due to nonspecific increased proliferation. The increased abundance in those tumor studies may instead indicate an increase in T cell fitness and survival in the TME. GS KO CD8$^+$ T cells also displayed increased mitochondrial content and a trend toward decreased mitochondrial potential (Fig. 2I), consistent with a memory phenotype and enhanced mitochondrial coupling or efficiency in the TME.[26]

Pharmacologic GS inhibition decreases CD8$^+$ T cell proliferation while increasing cytokine production in vitro

We next sought to evaluate the effects of pharmacologic inhibition of GS (GSi) using the compound L-methionine sulfoximine (MSO), a GS inhibitor that has been used extensively in neurodegenerative disease research.[27] WT CD8$^+$ T cells were activated in vitro in escalating doses of MSO over 72 h, and activation, proliferation, and viability were assessed by flow. While activation was unchanged, MSO treatment markedly reduced live cell count without reducing viability, suggesting a proliferative disadvantage (Fig. 3A, B). We directly assessed proliferation using CTV staining and found a significant reduction in replication index with MSO treatment (Fig. 3C). This effect may be a GS off-target effect of MSO, as T cell–specific GS KO did not appear to have proliferative defects (Fig. 2H). As with GS KO cells, cells activated in the presence of MSO showed a trend toward increased mitochondrial content and decreased membrane potential consistent with improved efficiency (Fig. 3D). Last, to assess effector function, cells were restimulated after 5 d of activation and analyzed for cytokine production. MSO treatment significantly increased the percentage of IFNγ and TNFα double positive cells (Fig. 3E, F), consistent with GSi enhancing CD8$^+$ T cell potential for antitumor function.

GS deficiency or inhibition increases intracellular glutamate and mitochondrial respiration

Because GS converts glutamate and ammonia to glutamine (Fig. 4A), we hypothesized that GS-deficient or GS-inhibited cells would have increased levels of intracellular glutamate to support glutamate-dependent metabolic processes. Indeed, when targeted metabolomics were performed on T cells activated in physiologic levels of glutamine, both GS KO and GSi treated CD8$^+$ T cells had a 2- to 5-fold increase in intracellular glutamate levels (Fig. 4B, C). While multiple metabolite levels were altered when comparing GS KO and WT cells, glutamate and aspartate accumulation were the most pronounced (Fig. 4D). Notably, GS KO cells maintained intracellular glutamine pools despite loss of GS, possibly due to increased glutamine uptake or decreased utilization.

To probe the mechanisms by which GS KO cells display a survival advantage in the TME, we next investigated the downstream cellular functions that utilize glutamate. One use for glutamate is as anaplerotic fuel for the TCA cycle. We hypothesized, therefore, that GS deficiency would support increased mitochondrial metabolism. Importantly, mitochondrial metabolism and respiratory capacity have been shown to be crucial for the development and maintenance of memory and stem-like CD8$^+$ population in tumors.[28–32] Indeed, GS KO CD8$^+$ T cells displayed increased basal and maximal mitochondrial respiration and increased spare respiratory capacity compared with WT counterparts in a mitochondrial stress test assay (Fig. 4E, F). Consistent with these findings, maximal respiration and spare respiratory capacity were also both markedly increased upon acute treatment of cells with MSO (Fig. 4G and H).

Deletion of GS enhances resistance to ROS

Another crucial cellular process that utilizes glutamate is the formation of the antioxidant GSH (Fig. 5A). As increased ROS can drive immunosuppression in the TME,[33,34] we tested if GS-deficiency altered T cell redox balance. In vitro activated GS KO CD8$^+$ T cells had significantly lower cellular ROS as measured by flow cytometry (Fig. 5B). Despite the increased mitochondrial respiration that supports ROS

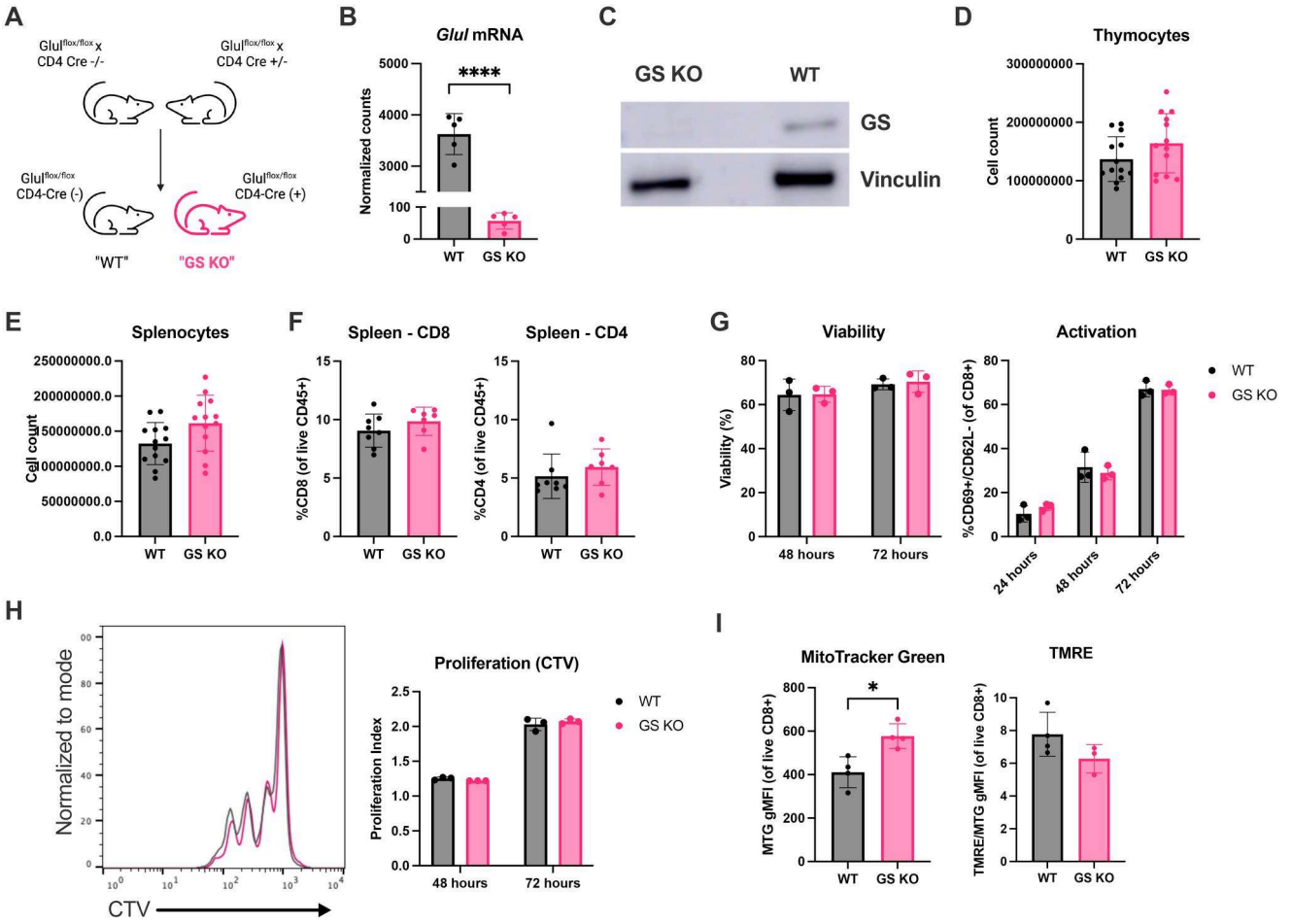

Figure 2. T cell specific GS deletion has no detrimental effects at baseline. (A) Breeding scheme for generation of T cell–specific GS KO vs WT littermate control mice. (B) *Glul* mRNA levels of WT vs GS KO CD8$^+$ T cells activated in vitro, as measured via bulk RNA sequencing and expressed as normalized counts following DESEQ2 analysis. n = 5 biological replicates. (C) Western blot showing GS and vinculin expression in cell lysates from activated WT vs GS KO CD8$^+$ T cells. (D) Live thymocytes and (E) splenocytes recovered from adult (8 wk) mice. Data from 2 experiments with 6 to 7 biological replicates each. (F) CD8$^+$ and CD4$^+$ T cells, reported as percentage of live CD45$^+$ cells, recovered from WT vs GS KO spleens. n = 7–8 biological replicates. (G) Viability and activation of recovered CD8$^+$ T cells from WT vs GS KO spleens, as measured by %CD69$^+$/CD62L$^-$, following 24, 48, and 72 h of activation in vitro with plate-bound anti-CD3/CD28. (H) CD8$^+$ T cell proliferation following ex vivo activation for 48 or 72 h, measured by CTV staining. Representative plot (left) and quantified proliferation index (right) with 3 biological replicates. (I) Geometric mean fluorescence intensity (gMFI) of activated WT vs GS KO CD8$^+$ T cells showing mitochondrial mass (MitoTracker Green) and mitochondrial membrane polarization (TMRE), normalized to mitochondrial mass. Statistically significant results are labeled. *$P < 0.05$, **$P < 0.01$, ***$P < 0.001$, ****$P \leq 0.0001$. Mann-Whitney test used in panels D to I.

formation, both GS KO CD8$^+$ T cells and WT cells activated in the presence of MSO showed decreased mitochondrial superoxides (Fig. 5C). Consistent with increased capacity to manage ROS, total and reduced GSH levels were increased when directly measured from cell lysates (Fig. 5D). Levels of GSSG, however, were unchanged, and the ratio of GSH: GSSG was increased. As this can serve as a proxy for the oxidative state of the cell, these levels are consistent with a low level of oxidative stress of GS-deficient T cells.

Overexpression of the rate-limiting enzyme in GSH synthesis in T cells, or direct supplementation with N-acetylcysteine, has been reported to enhance cell survival, memory formation, and overall antitumor immunity.[35,36] We therefore asked if GS KO CD8$^+$ cells were protected from external oxidative stress. When activated cells were incubated with increasing levels of hydrogen peroxide over a period of 3 h, WT cells displayed a marked and dose-dependent decrease in viability. While the highest concentrations also induced cell death in the GS KO CD8$^+$ cells, GS-deficient T cells were significantly more resistant to hydrogen peroxide (Fig. 5E). Importantly, WT cell viability was rescued with 1 mM GSH supplementation, while GS KO viability remained constant (Fig. 5F). These data provide another potential mechanism by which GS KO cells may have a fitness advantage in the TME through resistance to ROS stress.

GS deficient CD8$^+$ T cells have memory-like transcriptional changes and enhanced secondary recall in vivo

RNA sequencing was performed on ex vivo activated CD8$^+$ T cells from WT and GS KO mice to identify pathways that may contribute to the fitness advantage of GS KO T cells. Gene set enrichment analyses found metabolic pathways enriched in WT cells and DNA repair pathways enriched in GS KO (Fig. 6A). As increased DNA repair capacity is associated with immune memory[37] and CRISPR *Glul* KO TILs skewed toward the Tpex population in our earlier in vivo model (Fig. 1I, J), we specifically examined the gene signature of less differentiated hematopoietic stem cells. The Ivanova hematopoiesis stem cell long-term gene set[19] was significantly

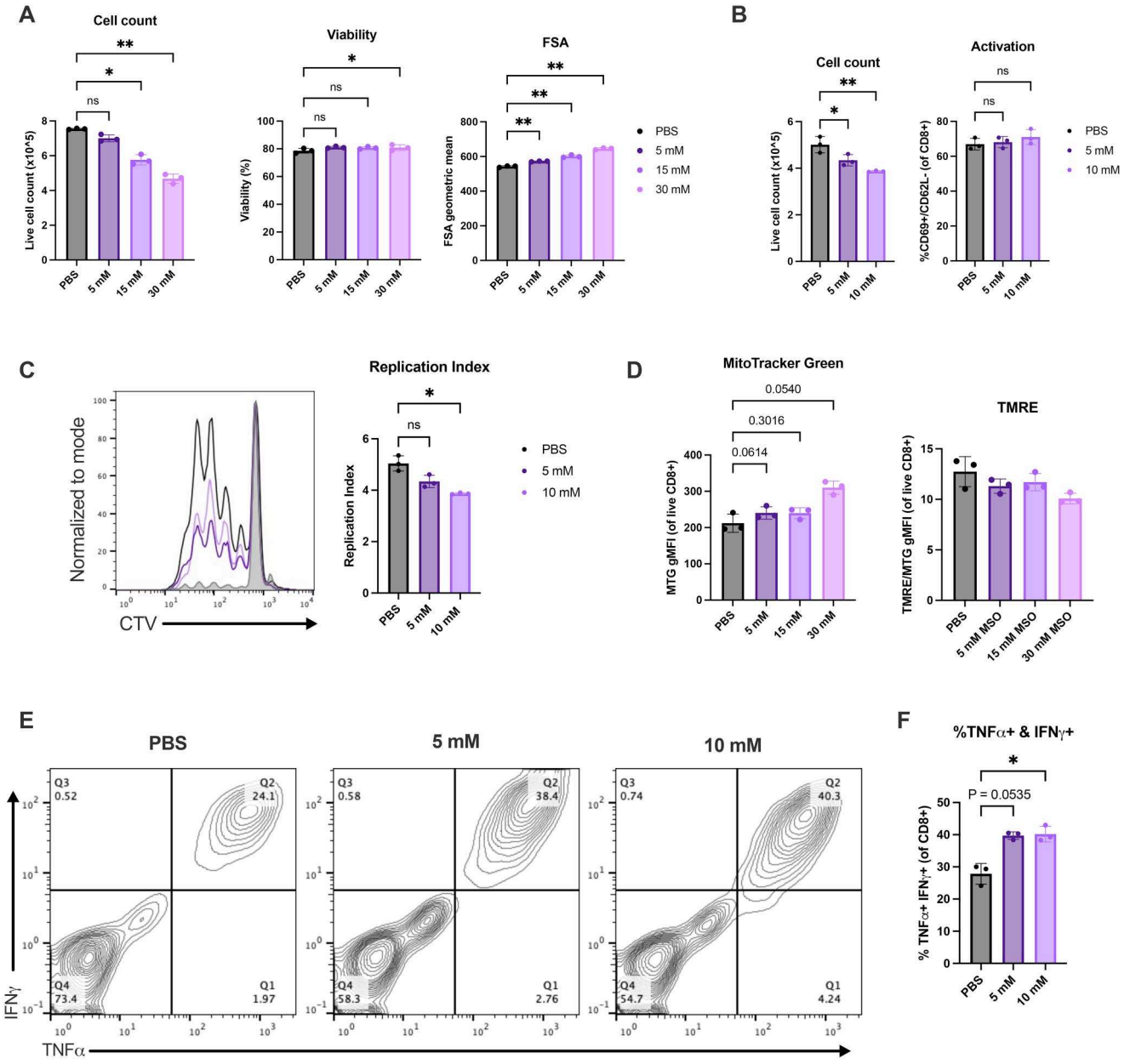

Figure 3. Pharmacologic GS inhibition alters cell proliferation while enhancing cytolytic capacity. (A) Isolated CD8$^+$ T cells activated in 0, 5, 15, or 30 mM MSO in vitro for 72 h. Live cell count, viability, and forward scatter (FSA) all measured via flow cytometry. n = 3 biological replicates. (B) Live cell count and percent CD62L$^-$/CD69$^+$ after 72 h of in vitro activation in 0, 5, or 10 mM MSO. n = 3 biological replicates. (C) Representative CTV histograms and replication index quantification on cells from panel B. n = 3. (D) MitoTracker Green and TMRE geometric MFI (gMFI) of cells activated for 72 h with increasing doses of MSO. TMRE normalized to mitochondrial content. n = 3. (E) Representative flow plots for TNFα and IFNγ production upon restimulation by cells activated in 0, 5, or 10 mM MSO, quantified in panel F. n = 3. Statistically significant results are labeled. *$P < 0.05$, **$P < 0.01$. One-way analysis of variance with Dunnett's multiple comparisons test used in panels A to D and F.

enriched in the GS KO cells compared with WT (Fig. 6B). While no differences were observed in levels of *pdcd1* mRNA encoding PD-1, recapitulating observations from surface expression of isolated TILs (Fig. 1K), GS KO cells displayed increased *tcf7* and *slamf6* mRNA levels and reduced *tox*, *lag3*, and *havcr2* (encoding Tim3) (Fig. 6C). These data suggest GS KO cells more closely approximate the transcriptional signature of precursor Tpex over terminally exhausted T cells (Tex), and may therefore retain functionality and proliferative capacity in an in vivo tumor context.[38]

To directly test the ability of GS KO cells to form memory populations and mount a secondary response upon rechallenge, mice were again injected with a 1:1 ratio of OT-I T cells transduced with either *Glul* or NTC sgRNAs. Mice were then infected with attenuated *L. monocytogenes* expressing SIINFEKL (*Lm*-Ova) on day 1 and 30 and bled 5 d later to measure the acute response or memory response, respectively (Fig. 6D). GS KO cells outcompeted NTC cells at both the acute (day 5) and memory (day 35) time point (Fig. 6E). The ratio of GS KO cells was significantly increased upon rechallenge, from an advantage of 1.3-fold to 5.1-fold enriched, suggesting an increase in persistence or recall ability of GS KO cells in comparison with the NTC CD8$^+$ T cells.

We next sought to directly test the memory response of GS KO cells in a tumor context. MC38-Ova tumor-bearing mice were treated with a curative dose of OT-I T cells in a 1:1 ratio

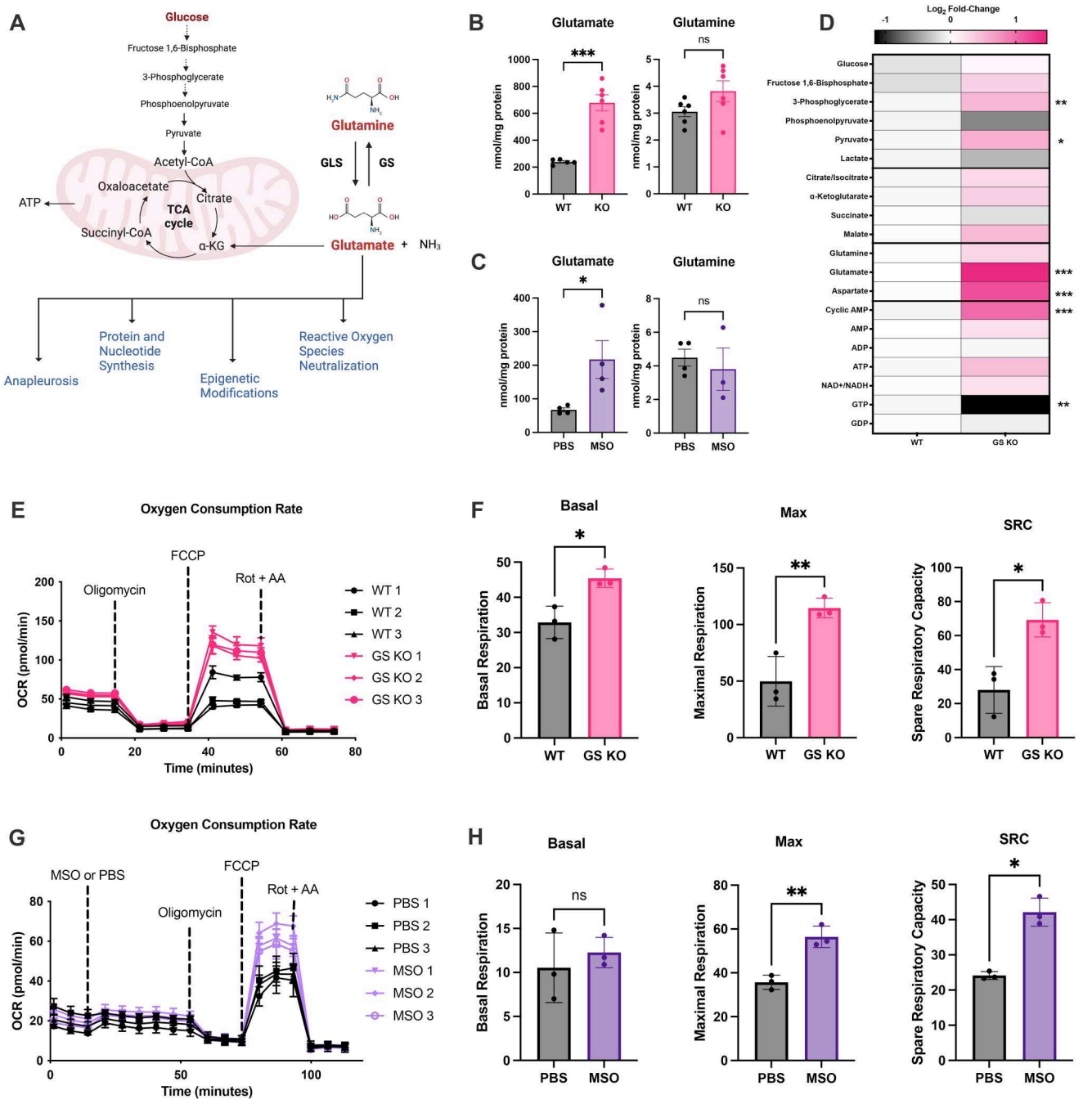

Figure 4. GS inhibition and KO increase glutamate and mitochondrial respiration. (A) Illustration showing glutamine utilization pathways. (B) Intracellular levels of glutamate and glutamine in activated CD8$^+$ T cells from WT or GS KO mice. n = 5 biological replicates. (C) Glutamate and glutamine levels in activated CD8$^+$ T cells treated for 48 h with MSO or vehicle control (PBS). n = 4 biological replicates. (D) Heatmap displaying log2 fold change of metabolites in WT vs GS KO CD8$^+$ T cells from panel B. (E) OCR tracing from MitoStress Test performed on activated CD8$^+$ T cells from WT or GS KO mice. Inhibitor injections labeled and marked with dashed lines. Each line represents a biological replicate, with 5 to 6 technical replicates each. (F) Quantification of basal respiration, maximal respiration, and spare respiratory capacity (SRC) of data shown in panel E. n = 3 biological replicates. (G) OCR tracing from MitoStress Test performed on activated CD8$^+$ T cells injected with either MSO or PBS. Dashed lines indicate time at which labeled inhibitors were injected. Each line represents a biological replicate, with n = 5-6 technical replicates. (H) Quantification of basal respiration, maximal respiration, and spare respiratory capacity (SRC) of data shown in panel G. n = 3 biological replicates. Statistically significant results are labeled. $^*P < 0.05$, $^{**}P < 0.01$, $^{***}P < 0.001$). Unpaired *t* test used in panels B to F, paired *t* test in panel G. AA, antimycin A (complex III inhibitor); Rot, rotenone (complex I inhibitor).

of GS KO:NTC. Mice were then rechallenged with MC38-Ova tumors on day 48 and bled periodically to observe the secondary response of transferred OT-I T cells (Fig. 6F). GS KO cells were more persistent than the NTC cells, with a 2.7-fold advantage prior to rechallenge, indicating an increased memory population formation and survival (Fig. 6G). Importantly, GS KO cells were more responsive and rapidly expanded to an 8-fold advantage upon tumor rechallenge. Notably, none of the mice developed tumors upon rechallenge and GS KO underwent normal contraction to a

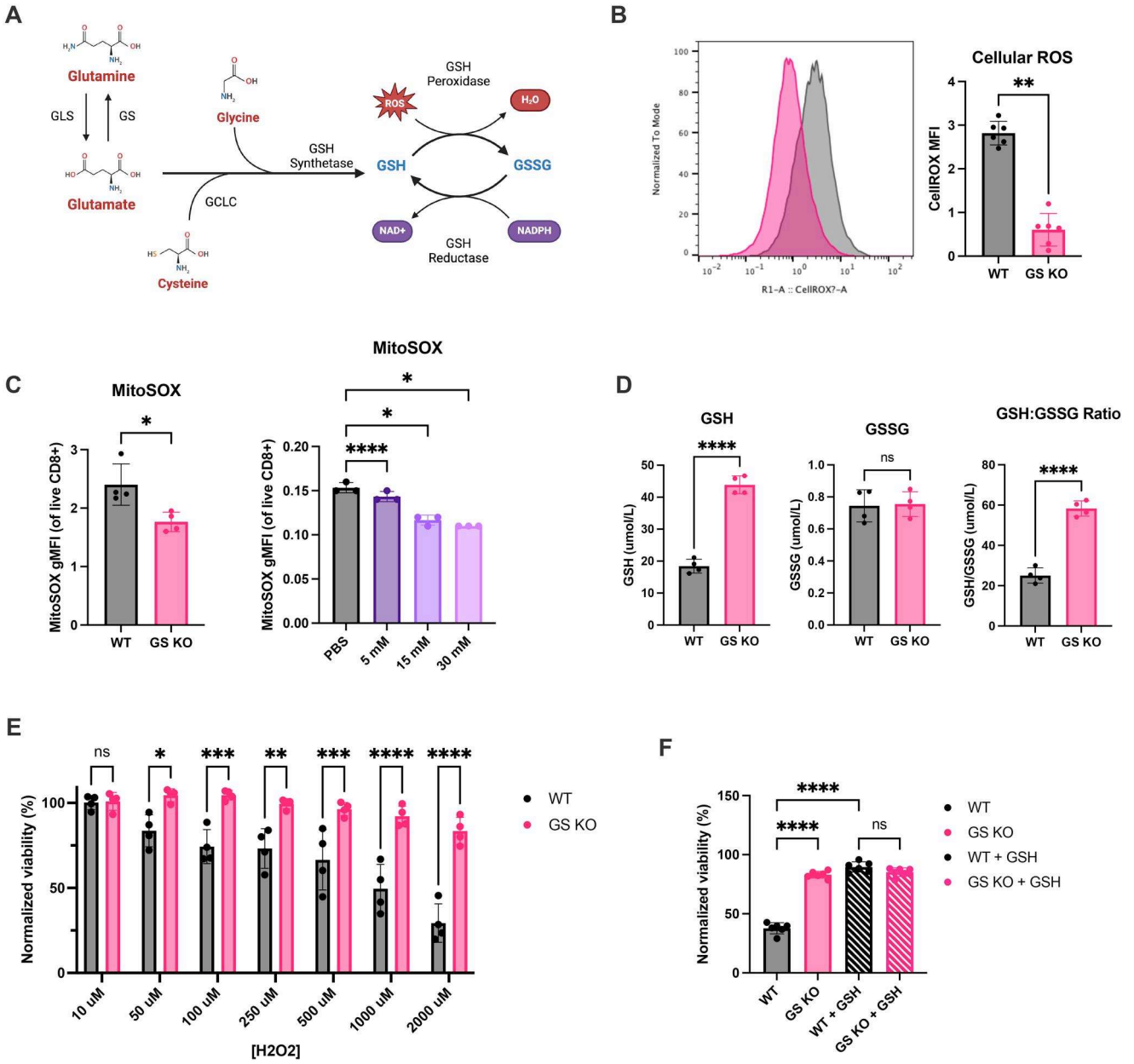

Figure 5. GS inhibition or KO increase cellular resistance to ROS. (A) Schematic showing pathway of glutamine fueling GSH antioxidant pools. Glutamine is converted to glutamate intracellularly, which is then used in the synthesis of GSH. GSH is oxidized into GSSG upon neutralization of cellular ROS by GSH peroxidase. (B) Cellular ROS as measured by CellROX staining on flow cytometry for anti-CD3/CD28 in vitro activated $CD8^+$ T cells from WT or GS KO mice. Representative histogram (left) and quantification (right). n = 6 biological replicates. (C) Mitochondrial ROS as measured by MitoSOX staining for WT vs GS KO $CD8^+$ T cells (left, n = 4) and cells activated in increasing doses of MSO (right, n =3). (D) Glutathione (reduced and oxidized) levels in activated $CD8^+$ T cells from WT vs GS KO mice. GSH = reduced glutathione. GSSG = oxidized glutathione. n = 4 biological replicates. (E) Viability as measured by flow cytometry of activated $CD8^+$ T cells from WT vs GS KO mice, following 3-h incubation with indicated concentrations of hydrogen peroxide. Viability was normalized to viability of cells cultured without hydrogen peroxide. n = 4 replicates. (F) Normalized viability for WT vs GS KO $CD8^+$ T cells incubated with 1,000 μM hydrogen peroxide, with and without supplementation with 1 mM GSH. n = 4 biological replicates. Statistically significant results are labeled. $^*P < 0.05$, $^{**}P < 0.01$, $^{***}P < 0.001$, $^{****}P \leq 0.0001$). Unpaired *t* test used in panels B to D, 1-way analysis of variance in with multiple comparisons in panels C and F, and 2-way analysis of variance in panel E.

2.8-fold advantage that was similar to prechallenge frequencies by day 12 postinjection.

Targeting GS enhances antitumor immunity in multiple orthotopic tumor models

To test if pharmacologic GS inhibition protects against tumors in an in vivo model, we treated mice with daily intraperitoneal injections of 20 mg/kg MSO or PBS control for 5 consecutive d starting on day 10 after injection with the HKP1-Ova-luciferase orthotopic lung adenocarcinoma model (Fig. 7A). Treatment with MSO significantly reduced tumor burden as measured by bioluminescent imaging and lung mass at endpoint (Fig. 7B–D). As MSO has been previously reported to have a proinflammatory effect on tumor-associated macrophages,[39] we analyzed the tumor-infiltrating $CD8^+$ T cells to evaluate the T cell–specific effects of in vivo MSO treatment on the T cells specifically.

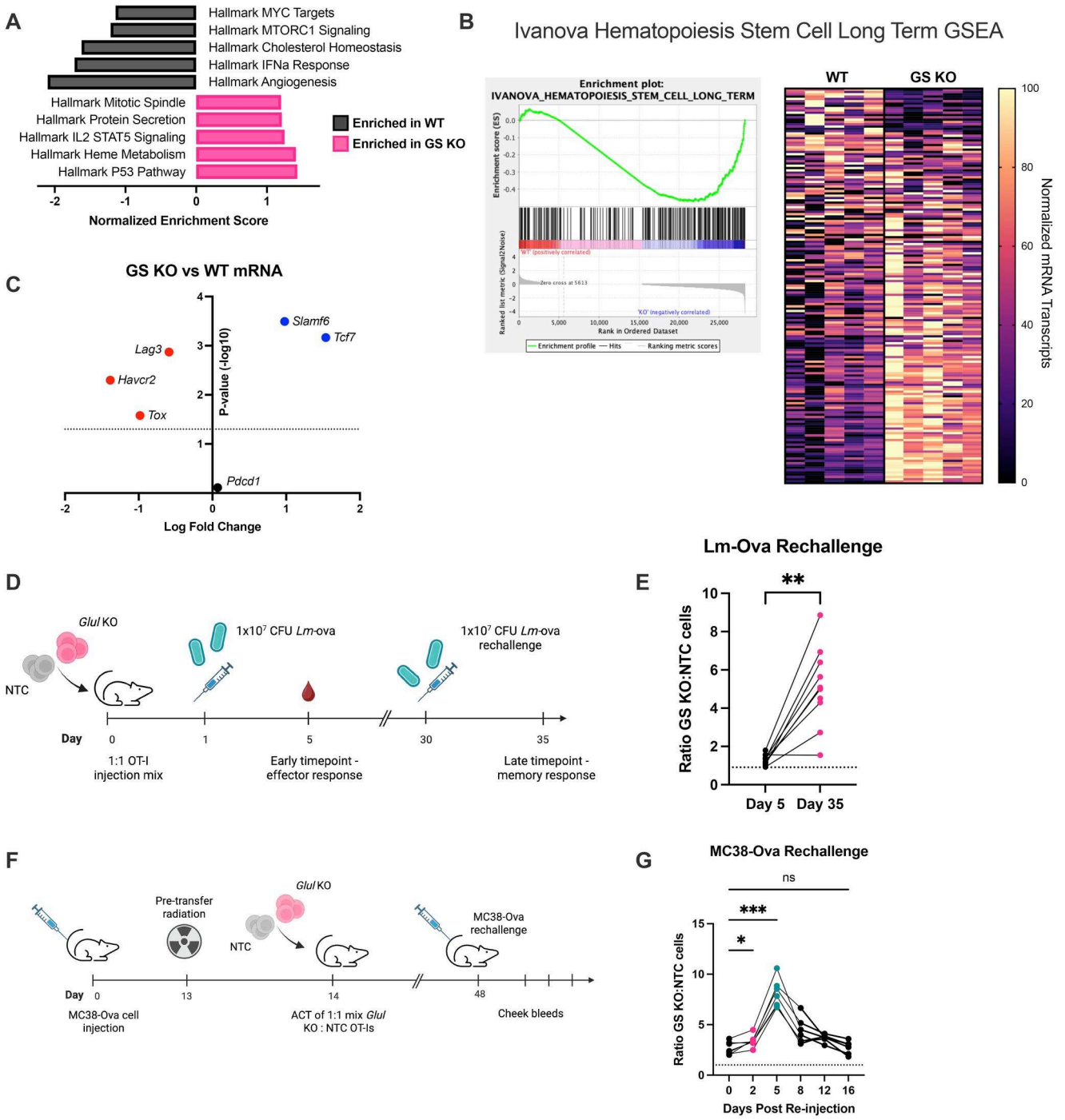

Figure 6. GS KO enhances the memory transcriptional profile and recall ability of CD8$^+$ T cells. (A) Normalized enrichment score of top 5 differentially expressed hallmark pathways for WT (black) vs GS KO (pink) CD8$^+$ T cells following GSEA. n = 5 biological replicates. (B) GSEA plot for Ivanova hematopoiesis stem cell long-term gene set (right, $P < 0.0001$) and heatmap showing normalized mRNA levels for genes included in set (left). (C) Volcano plot showing log fold change and −log10(*P* value) for *pdcd1, tcf7, tox, lag3, slamf6,* and *havcr2* mRNA, as measured by bulk RNA sequencing and analyzed with DESeq2. Dotted line corresponds to a *P* value of 0.05. (D) Schematic showing timeline for *Lm*-Ova rechallenge experiment. (E) Ratio of GS KO to NTC OT-I T cells in mice infected with *Lm*-Ova on day 5 (acute response) and 35 (secondary recall response). The dotted line represents the ratio of GS KO: NTC cells at time of adoptive T cell therapy the day prior to *Lm*-Ova infection (0.909). (F) Schematic showing methodology for MC38-Ova tumor rechallenge experiment. (G) Ratio of GS KO to NTC OT-I T cells in mice rechallenged with MC388-Ova tumors. Dotted line represents ratio of GS KO:NTC cells on the day of adoptive T cell therapy (1.005). Statistically significant results are labeled. $^*P < 0.05$, $^{**}P < 0.01$, $^{***}P < 0.001$). Paired Wilcoxon test in panel E), Wilcoxon matched-pairs signed rank test used in panel E), repeated measures 1-way analysis of variance with multiple comparisons in panel G).

MSO treatment significantly increased the percentage of infiltrating CD8$^+$ T cells as well as their ability to produce TNFα and IFNγ upon restimulation ex vivo, without a significant change in PD-1 expression (Fig. 7E–H).

We next sought to test if the treatment benefit observed with MSO was broadly applicable and utilized the PyMT orthotopic breast cancer model (Fig. 8A). Again, MSO treatment reduced tumor burden as measured by tumor volume

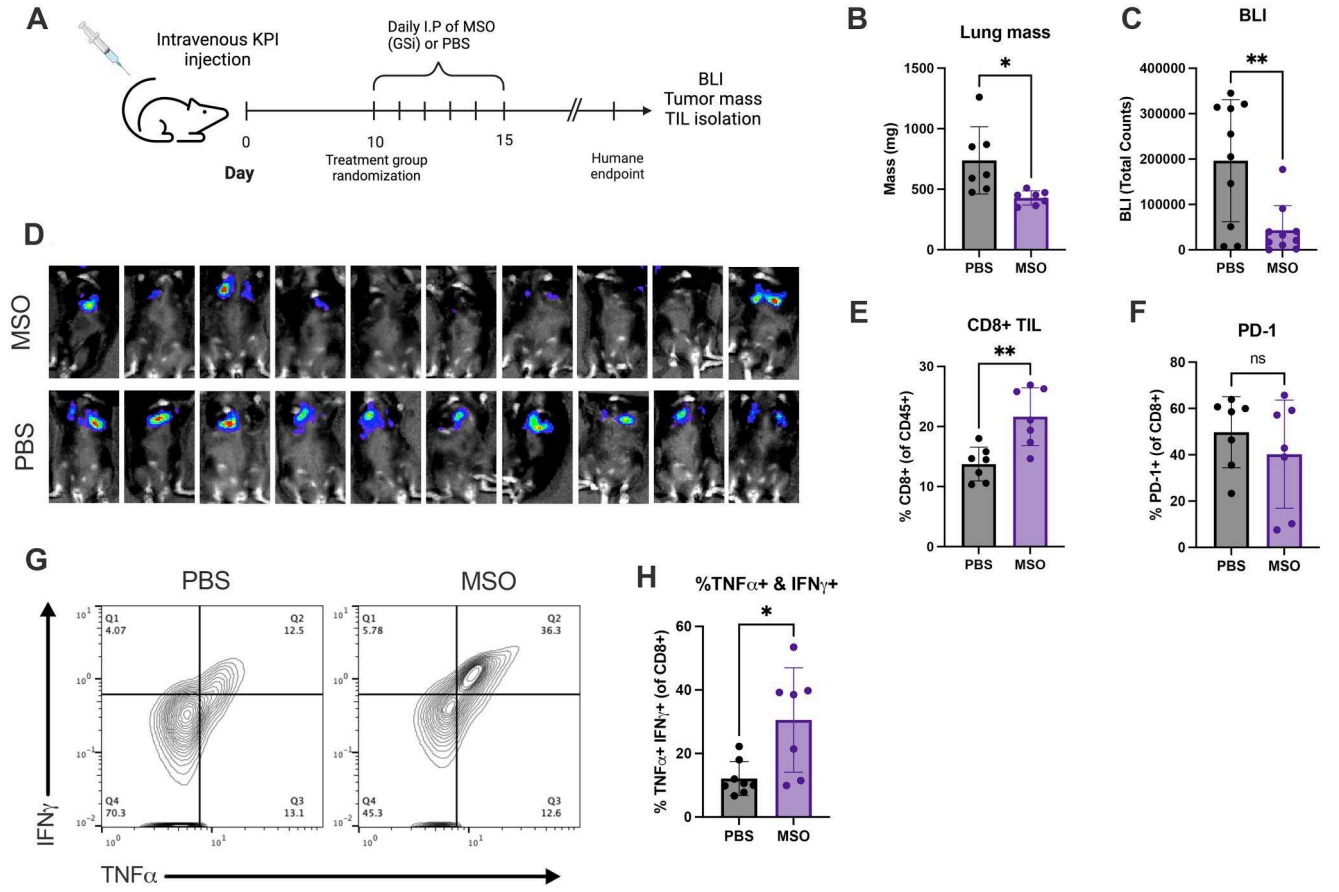

Figure 7. GS inhibition enhances CD8$^+$ T cells infiltration and improves tumor control in vivo. (A) Schematic showing experimental protocol for results in panels B to H, n = 10 biological replicates. (B) Lung mass as a proxy for tumor burden. (C) Quantification of total bioluminescence immediately prior to sacrifice. (D) Images used for the quantification in panel C). (E) Percentage of infiltrating CD8$^+$ T cells in tumors from PBS- vs MSO-treated mice, reported as percentage of CD45$^+$ cells. (F) Percentage of PD-1$^+$ CD8$^+$ T cells, as measured by flow. (G) Representative flow plots showing IFNγ and TNFα production from recovered TILs following 3-h restimulation with PMA and ionomycin. (H) Percentage of IFNγ and TNFα double positive population. Statistically significant results are labeled. $^*P < 0.05$, $^{**}P < 0.01$. Unpaired *t* test used in panels B, C, E, F, and H.

and mass (Fig. 8B, C). Importantly, MSO treatment did not reduce tumor burden when PyMT cells were injected into immunodeficient *Rag1*$^{-/-}$ mice, indicating a crucial role for the adaptive immune response in the antitumor efficacy of MSO (Fig. 8D). Furthermore, CD8$^+$ T cells were enriched following MSO treatment in the breast tumor tissue and displayed increased cytokine production (Fig. 8E, F). Notably, while PD-1 surface expression was again unchanged, TILs recovered from MSO treated mice displayed a marked increase in TCF-1$^+$ and decrease in TOX$^+$ populations (Fig. 8G, H). TCF-1$^+$TOX$^-$ TIL populations have been associated with Tpex cells, while TOX$^+$TCF-1$^-$ populations reflect terminally exhausted Tex. These data are consistent with mRNA levels of TOX, TCF, and surface exhaustion markers from in vitro RNA sequencing data (Fig. 2L), as well as data showing increased mitochondrial respiration and decreased ROS. Together, these data show GS inhibition can enhance T cell mitochondrial and oxidative resilience and promote Tpex over Tex formation.[33,35,36]

Discussion

Targeting glutamine metabolism may provide a means to enhance T cell function in the TME. In this study, we sought to identify the enzymatic target responsible for the enhancement of CD8$^+$ T cell function seen with DON therapy and determine if precision targeting of this enzyme could recapitulate the antitumor effects. Using a targeted CRISPR screen, we found that GS deficiency conferred a survival advantage to CD8$^+$ T cells in the TME. Targeting GS demonstrated robust antitumor effects in multiple models. In vivo treatment with a GS inhibitor (MSO) also reduced tumor burden in both orthotopic lung and breast cancer models, accompanied by increased infiltration and improved functionality of CD8$^+$ T cells. Importantly, GS inhibition promoted the formation of Tpex over Tex, a critical shift to maintain effective and durable antitumor immunity.[38]

Previous work in our lab and others has focused on glutaminase (GLS), the first and rate-limiting enzyme in glutaminolysis, which catalyzes the reverse reaction of GS. Inhibiting GLS enhanced T helper 1 (Th1) differentiation and function over Th17 cells while also improving cytokine production in CD8$^+$ T cells.[40] This effect may be driven by a compensatory increase in glycolysis upon glutaminolysis inhibition, promoting effector function in CD8$^+$ T cells. However, GLS inhibition also led to an increase in inhibitory molecule expression in CD8$^+$ T cells, suggesting a highly activated, terminally differentiated phenotype.[41] While these cells exhibit enhanced cytolytic activity, they may have reduced persistence and survival in the TME—an idea supported by the lack of enrichment of GLS-targeted cells in our CRISPR screen.

The GLS inhibitor CB-839 has progressed to clinical trials as a potential antitumor therapy in combination with

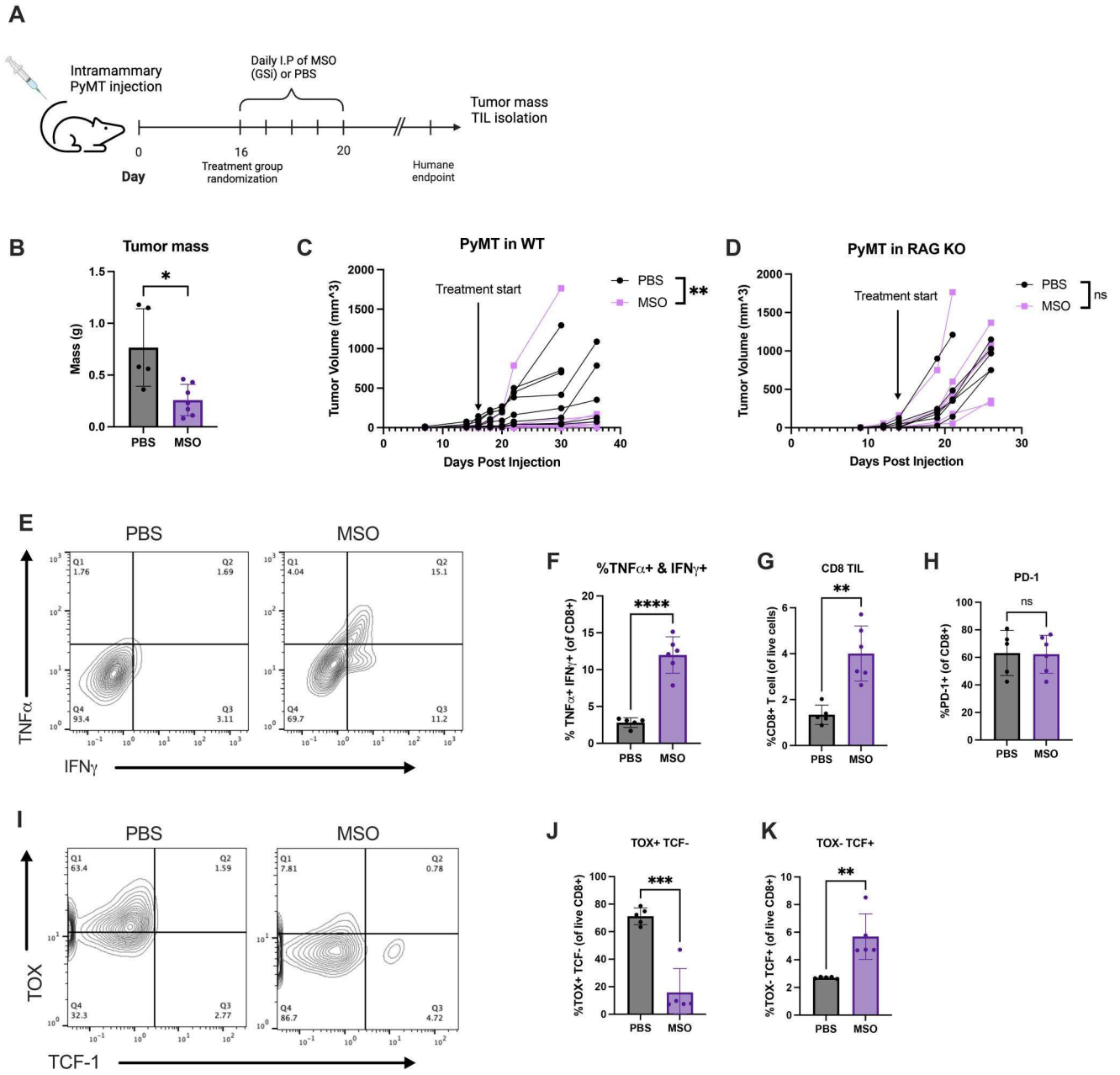

Figure 8. GS inhibition enhances adoptive T cell therapy efficacy in breast cancer model. (A) Schematic of experimental protocol for results in panels B to J. (B) Growth curve for tumors in mice treated with MSO (purple) vs PBS (black). n = 8 for both groups at start of experiment, 4 mice (3 PBS and 1 MSO) required euthanasia prior to study endpoint. (C) Tumor mass at study endpoint for mice treated with MSO vs PBS. n = 5–7 replicates. (D) Growth curve for PyMT tumors in *Rag1*$^{-/-}$ mice treated with MSO (purple) vs PBS (black). n = 6 biological replicates each. (E) Representative flow plots showing IFNγ and TNFα production from recovered TILs following 3-h restimulation with PMA and ionomycin. n = 5–7 replicates, quantified in panel F. (G) Percentage of infiltrating CD8$^+$ T cells in tumors from PBS- vs MSO-treated mice, reported as percentage of CD45$^+$ cells. n = 5–7. (H) Percentage of PD-1$^+$ CD8$^+$ T cells, as measured by flow. n = 5–7. (I) Representative flow plots showing TOX$^+$ and TCF-1$^+$ populations, gated on live CD8$^+$ T cells and quantified in panels J and K. n = 5–7. Statistically significant results are labeled. *$P < 0.05$, **$P < 0.01$, ***$P < 0.001$, ****$P \leq 0.0001$). Unpaired *t* test used in panels B, F to H, J, and K.

checkpoint inhibitors, aiming to counteract the increased expression of exhaustion markers. However, early-phase clinical trials in metastatic renal cell carcinoma in combination with checkpoint inhibition have shown limited efficacy.[42] Interestingly, GLS is now being explored as a target for anti-inflammatory therapies, having demonstrated efficacy in a preclinical model of rheumatoid arthritis.[43] In contrast, GS inhibition shifted cells toward oxidative phosphorylation rather than glycolysis. While GS-deficient cells retained the ability to produce cytokines upon restimulation, they exhibited a less activated, less differentiated phenotype. Notably, both GS and GLS—the enzymatic target of CB-839—operate at the same metabolic junction, regulating the conversion between glutamine and glutamate.[40,41,44] This suggests that metabolic flexibility between these intermediates may be critical for T cell fitness in tumors, aligning with the variable glutamine levels observed in the TME.[45]

Previous work has identified GS as a potential antitumor therapeutic target in macrophages, with studies suggesting GS inhibition leads to increased proinflammatory M1-like macrophages.[39] Notably, the observed antitumor effect was dependent on CD8$^+$ T cell recruitment and function in these

studies. Additionally, GS may act as a scaffolding protein involved in licensing mitotic progression in multiple tumor xenograft models, independent of its metabolic function.[46] Similar results from MSO-mediated inhibition of GS enzymatic function, however, suggest an enzymatic role for GS-regulation of T cell fate. Our work adds to the current literature by detailing the intrinsic effects of GS KO on $CD8^+$ T cells. Targeting a protein crucial for tumor cell function that is simultaneously detrimental to inflammatory macrophage and cytolytic T cell activity make GS an attractive target for future investigation in cellular immunotherapies.

A defining feature of the TME is the limited availability of nutrients, including glutamine, which is essential for both tumor and immune cell metabolism. Our results suggest that GS deficiency may enable $CD8^+$ T cells to adapt to this nutrient-scarce environment by preserving and increasing intracellular glutamate levels. We observed enhanced mitochondrial content and respiratory capacity in GS KO cells and those treated with MSO. Consistent with our findings, recent studies have highlighted the importance of mitochondrial metabolism and flexibility to maintain $CD8^+$ T cell antitumor immunity and formation of long-lived memory and progenitor-like populations.[26,47,48] Intracellular glutamate also serves as a precursor for the antioxidant GSH. We observed elevated GSH levels in GS-deficient cells, which enhanced resistance to oxidative stress. Importantly, previous studies have shown that antioxidant capacity is essential for the survival and function of long-lived progenitor T cells, particularly during chronic antigen stimulation.[30,33,35,36] As mitochondrial metabolism is a major source of oxidative stress,[49] GS KO cells may be able to increase mitochondrial metabolism to a greater degree given their ability to neutralize the resulting oxidative stress. These findings align with prior work highlighting the interplay between redox balance and T cell fitness in the TME.

While our study highlights the therapeutic promise of GS inhibition, it also raises important questions for future investigation. First, the mechanisms by which GS-deficient T cells maintain intracellular glutamine pools remain unclear. Potential compensatory mechanisms, such as increased glutamine uptake or reduced utilization, should be assessed. Additionally, the long-term effects of GS inhibition on T cell memory, persistence, and secondary recall should be evaluated, particularly under conditions of chronic antigen stimulation in tumors. Finally, the impact of GS inhibition on other immune and stromal cells in the TME warrants further study, given the established influence of glutamine metabolism on multiple cell types in this environment.[39,46] Our findings identify GS as a key metabolic regulator of $CD8^+$ T cell fitness in the TME. GS inhibition reprograms T cell metabolism to favor mitochondrial respiration and antioxidant production, improving persistence, functionality, and resistance to oxidative stress. These insights deepen our understanding of the mechanisms underlying DON therapy and establish GS as a promising therapeutic target for enhancing immune-based cancer treatments.

Acknowledgments

The authors thank Richard O'Neil for the MC38-Ova cell line, the Ann Richmond lab for PyMT cells, and Vivek Mittal at the Weill Cornell Medicine Graduate School of Medical Sciences for generously gifting the HKP1-Ova cell line. Cryopreserved sperm of *Glul* fl/fl mice were generously gifted from Saverio Tardito at the University of Glasgow School of Cancer Sciences. IVF rederivation was performed by the Vanderbilt Genome Editing Resource. Additional technical assistance was provided by the Vanderbilt Translational Pathology Shared Resource, the VANTAGE core, and the Vanderbilt University Medical Center Flow Cytometry Shared Resource. Diagrams were created in BioRender. The National Institutes of Health Tetramer facility provided SIINFEKL-specific tetramer.

Author contributions

E.L.F.-G. (Conceptualization [Equal], Data curation [Equal], Formal analysis [Equal], Investigation [Equal], Methodology [Equal], Validation [Equal], Visualization [Equal], Writing—original draft [Equal], Writing—review & editing [Equal]), E. S.H. (Investigation [Equal], Methodology [Equal]), J.M.P. (Investigation [Equal]), E.Q.J. (Formal analysis [Equal], Investigation [Equal], Methodology [Equal]), C.C. (Investigation [Equal]), A.E.S. (Investigation [Equal]), S.H.S. (Investigation [Equal]), J.E.M. (Investigation [Equal]), R.C.S. (Investigation [Equal]), J.A.D. (Investigation [Equal], Methodology [Equal]), H.C. (Formal analysis [Equal]), J.T. W. (Resources [Equal], Supervision [Equal]), J.M. (Supervision [Equal]), and J.C.R. (Conceptualization [Equal], Funding acquisition [Equal], Project administration [Equal], Resources [Equal], Supervision [Equal], Writing—review & editing [Equal])

Funding

This work was supported by theNational Institute of General Medical Sciences grant T32 GM007347 (to E.L.F.-G., C.C., and J.A.D.);National Institute of Allergy and Infectious Diseases grants F31 AI186436 (to R.C.S.) and T32 AI112341 (to R.C.S.),National Cancer Institute grants T32 CA009592 (to S.H.S.), R01 CA266767 (to J.T.W.), R01 CA274675 (to J.T.W.), and R01 CA217987 (to J.C.R.); National Institute of Diabetes and Digestive and Kidney Diseases grant R01 DK105550 (to. J.C.R.); theMark Foundation for Cancer Research Endeavor (to J.C.R.); Department of Defense Congressionally Directed Medical Research Program CA240991P1 (to J.C.R.); and the Waddell Walker Hancock Cancer Discovery Scholar Award (to J.C.R. and J.T.W.). The Vanderbilt Genome Editing Resource, Vanderbilt Translational Pathology Shared Resource, and Vanderbilt University Medical Center Flow Cytometry Shared Resource (FCSR) cores are supported by theNational Cancer Institute/National Institutes of Health Cancer Center Support Grant P30 CA068485. The FCSR core is additionally supported by theVanderbilt Digestive Disease Research Center (P30 DK058404).

Conflicts of interest

J.C.R. is a founder and scientific advisory board member for Sitryx Therapeutics. The other authors have no financial conflicts of interest.

References

1. Finck AV, Blanchard T, Roselle CP, Golinelli G, June CH. Engineered cellular immunotherapies in cancer and beyond. Nat Med. 2022;28:678–689.
2. Food and Drug Administration. FDA Approves First Cellular Therapy to Treat Patients with Unresectable or Metastatic Melanoma. 2024. Accessed October 16, 2025. https://www.fda.gov/news-events/press-announcements/fda-approves-first-cellular-therapy-treat-patients-unresectable-or-metastatic-melanoma
3. Hou AJ, Chen LC, Chen YY. Navigating CAR-T cells through the solid-tumour microenvironment. Nat Rev Drug Discov. 2021;20:531–550.
4. Heintzman DR, Fisher EL, Rathmell JC. Microenvironmental influences on T cell immunity in cancer and inflammation. Cell Mol Immunol. 2022;19:316–326.
5. Ho P-C et al. Phosphoenolpyruvate is a metabolic checkpoint of anti-tumor T cell responses. Cell. 2015;162:1217–1228.
6. DePeaux K, Delgoffe GM. Metabolic barriers to cancer immunotherapy. Nat Rev Immunol. 2021;21:785–797.
7. Magill GB et al. Pharmacological and initial therapeutic observations on 6-diazo-5-oxo-1-norleucine (DON) in human neoplastic disease. Cancer. 1957;10:1138–1150.
8. Rais R et al. Discovery of 6-diazo-5-oxo-l-norleucine (DON) prodrugs with enhanced CSF delivery in monkeys: a potential treatment for glioblastoma. J Med Chem. 2016;59:8621–8633.
9. Tenora L et al. Tumor-targeted delivery of 6-diazo-5-oxo-l-norleucine (DON) using substituted acetylated lysine prodrugs. J Med Chem. 2019;62:3524–3538.
10. Oh M-H et al. Targeting glutamine metabolism enhances tumor-specific immunity by modulating suppressive myeloid cells. J Clin Invest. 2020;130:3865–3884.
11. Praharaj M et al. Metabolic reprogramming of tumor-associated macrophages using glutamine antagonist JHU083 drives tumor immunity in myeloid-rich prostate and bladder cancers. Cancer Immunol Res. 2024;12:854–875.
12. Xu H et al. Azo-based hypoxic-activated 6-diazo-5-oxo-L-norleucine (DON) prodrug combined with vascular disrupting agent nanoparticles for tumor-selective glutamine metabolism blockade. Chem Eng J. 2024;481:148281.
13. Leone RD et al. Glutamine blockade induces divergent metabolic programs to overcome tumor immune evasion. Science. 2019;366:1013–1021.
14. Villar VH et al. Hepatic glutamine synthetase controls N(5)-methylglutamine in homeostasis and cancer. Nat Chem Biol. 2023;19:292–300.
15. Madden MZ et al. Differential effects of glutamine inhibition strategies on antitumor CD8 T cells. J Immunol. 2023;211:563–575.
16. Choi H et al. Transcriptome analysis of individual stromal cell populations identifies stroma-tumor crosstalk in mouse lung cancer model. Cell Rep. 2015;10:1187–1201.
17. Sugiura A et al. Tissue-specific dependence of Th1 cells on the amino acid transporter SLC38A1 in inflammation [preprint], bioRxiv 2023:557496. https://doi.org/10.1101/2023.09.13.557496
18. Li W et al. MAGeCK enables robust identification of essential genes from genome-scale CRISPR/Cas9 knockout screens. Genome Biol. 2014;15:554.
19. Ivanova NB et al. A stem cell molecular signature. Science. 2002;298:601–604.
20. Subramanian A et al. Gene set enrichment analysis: a knowledge-based approach for interpreting genome-wide expression profiles. Proc Natl Acad Sci U S A. 2005;102:15545–15550.
21. Castanza AS et al. Extending support for mouse data in the Molecular Signatures Database (MSigDB). Nat Methods. 2023;20:1619–1620.
22. FIGS: Functional ImmunoGenomics reSource. 2024. Accessed October 16, 2025. https://functionalimmunogenomics.shinyapps.io/crispr/
23. Lemberg KM, Vornov JJ, Rais R, Slusher BS. We're not "DON" yet: optimal dosing and prodrug delivery of 6-diazo-5-oxo-l-norleucine. Mol Cancer Ther. 2018;17:1824–1832.
24. Viswanath P et al. A novel method for quantifying total thoracic tumor burden in mice. Neoplasia. 2018;20:975–984.
25. Cruzat V, Macedo Rogero M, Noel Keane K, Curi R, Newsholme P. Glutamine: metabolism and immune function, supplementation and clinical translation. Nutrients. 2018;10:1564.
26. Scharping NE et al. The tumor microenvironment represses T cell mitochondrial biogenesis to drive intratumoral T cell metabolic insufficiency and dysfunction. Immunity. 2016;45:374–388.
27. Ghoddoussi F et al. Methionine sulfoximine, an inhibitor of glutamine synthetase, lowers brain glutamine and glutamate in a mouse model of ALS. J Neurol Sci. 2010;290:41–47.
28. van der Windt GJW et al. Mitochondrial respiratory capacity is a critical regulator of CD8+ T cell memory development. Immunity 2012;36:68–78.
29. Siska PJ et al. Mitochondrial dysregulation and glycolytic insufficiency functionally impair CD8 T cells infiltrating human renal cell carcinoma. JCI Insight. 2017;2:e93411.
30. Vardhana SA et al. Impaired mitochondrial oxidative phosphorylation limits the self-renewal of T cells exposed to persistent antigen. Nat Immunol. 2020;21:1022–1033.
31. Yu Y-R et al. Disturbed mitochondrial dynamics in CD8(+) TILs reinforce T cell exhaustion. Nat Immunol. 2020;21:1540–1551.
32. Scharping NE et al. Mitochondrial stress induced by continuous stimulation under hypoxia rapidly drives T cell exhaustion. Nat Immunol. 2021;22:205–215.
33. Chen X, Song M, Zhang B, Zhang Y. Reactive oxygen species regulate T cell immune response in the tumor microenvironment. Oxid Med Cell Longev. 2016;2016:1580967.
34. Abbott KL et al. Metabolite profiling of human renal cell carcinoma reveals tissue-origin dominance in nutrient availability. Elife. 2024;13:RP95652.
35. Pilipow K et al. Antioxidant metabolism regulates CD8+ T memory stem cell formation and antitumor immunity. JCI Insight. 2018;3:e122299.
36. Lancien M et al. Cystathionine-gamma-lyase overexpression in T cells enhances antitumor effect independently of cysteine autonomy. Cancer Sci. 2021;112:1723–1734.
37. Johnnidis JB et al. Inhibitory signaling sustains a distinct early memory CD8(+) T cell precursor that is resistant to DNA damage. Sci Immunol. 2021;6:eabe3702.
38. Kallies A, Zehn D, Utzschneider DT. Precursor exhausted T cells: key to successful immunotherapy? Nat Rev Immunol. 2020;20:128–136.
39. Palmieri EM et al. Pharmacologic or genetic targeting of glutamine synthetase skews macrophages toward an M1-like phenotype and inhibits tumor metastasis. Cell Rep. 2017;20:1654–1666.
40. Johnson MO et al. Distinct regulation of Th17 and Th1 cell differentiation by glutaminase-dependent metabolism. Cell. 2018;175:1780–1795.e19.
41. Byun J-K et al. Inhibition of glutamine utilization synergizes with immune checkpoint inhibitor to promote antitumor immunity. Mol Cell. 2020;80:592–606.e8.
42. Tannir NM et al. CANTATA: Primary analysis of a global, randomized, placebo (Pbo)-controlled, double-blind trial of telaglenastat (CB-839) + cabozantinib versus Pbo + cabozantinib in advanced/metastatic renal cell carcinoma (mRCC) patients (pts) who progressed on immune checkpoint inhibitor (ICI) or anti-angiogenic therapies. J Clin Oncol. 2021;39:4501.
43. Ahmed S et al. Dual inhibition of glycolysis and glutaminolysis for synergistic therapy of rheumatoid arthritis. Arthritis Res Ther. 2023;25:176.

44. Varghese S et al. The glutaminase inhibitor CB-839 (Telaglenastat) enhances the antimelanoma activity of T-Cell-Mediated immunotherapies. Mol Cancer Ther. 2021;20:500–511.
45. Cluntun AA, Lukey MJ, Cerione RA, Locasale JW. Glutamine metabolism in cancer: understanding the heterogeneity. Trends Cancer. 2017;3:169–180.
46. Zhao J-S et al. Glutamine synthetase licenses APC/C-mediated mitotic progression to drive cell growth. Nat Metab. 2022;4:239–253.
47. Buck MD et al. Mitochondrial dynamics controls T cell fate through metabolic programming. Cell. 2016;166:63–76.
48. Chen Cet al. Mitochondrial metabolic flexibility is critical for CD8+ T cell antitumor immunity. Sci Adv. 2023; 9:eadf9522.
49. Heintzman DR et al. Subset-specific mitochondrial stress and DNA damage shape T cell responses to fever and inflammation. Sci Immunol. 2024;9:eadp3475.

The Journal of Immunology, 2025, 00, 1–17
https://doi.org/10.1093/jimmun/vkaf250
Research Article